Electric Field-Induced Emission Enhancement and Modulation in Individual CdSe Nanowires

Felix Vietmeyer,[†] Tamar Tchelidze,[‡,§] Veronica Tsou,[†,⊥] Boldizsar Janko,[‡] and Masaru Kuno[†,*]

[†]Department of Chemistry and Biochemistry and [‡]Department of Physics, University of Notre Dame, Notre Dame, Indiana 46556, United States, [§]Faculty of Exact and Natural Sciences, Iv. Javakhishvili Tbilisi State University, 0179 Tbilisi, Georgia, and [⊥]Nanotechnology Engineering, University of Waterloo, Waterloo, Ontario N2L 3G1, Canada

ABSTRACT

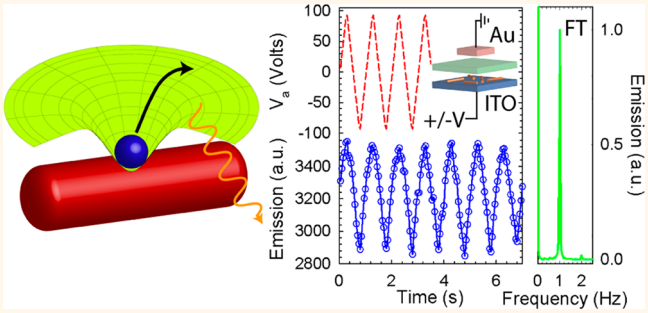

CdSe nanowires show reversible emission intensity enhancements when subjected to electric field strengths ranging from 5 to 22 MV/m. Under alternating positive and negative biases, emission intensity modulation depths of 14 ± 7% are observed. Individual wires are studied by placing them in parallel plate capacitor-like structures and monitoring their emission intensities *via* single nanostructure microscopy. Observed emission sensitivities are rationalized by the field-induced modulation of carrier detrapping rates from NW defect sites responsible for nonradiative relaxation processes. The exclusion of these states from subsequent photophysics leads to observed photoluminescence quantum yield enhancements. We quantitatively explain the phenomenon by developing a kinetic model to account for field-induced variations of carrier detrapping rates. The observed phenomenon allows direct visualization of trap state behavior in individual CdSe nanowires and represents a first step toward developing new optical techniques that can probe defects in low-dimensional materials.

KEYWORDS: semiconductor · CdSe · nanowire · emission intensity modulation · defects · Poole–Frenkel effect · phonon-assisted tunneling

Defects are an important and unavoidable feature of all materials. In semiconductors, they play a key role in dictating their optical and electrical response. For example, they define time scales for nonradiative decay processes. They also affect a material's transport properties either through carrier capture or by acting as scattering centers. This connection between a system's optical/electrical properties and defects was established more than 50 years ago.[1] Since then, strategies have been developed to precisely tailor material properties by reducing/manipulating these defects. This has, in turn, catalyzed the rapid development of modern electronics.

Defect investigations are even more relevant today with the advent of nanoscale materials. This is because a large fraction of atoms reside at the surface of nanostructures given their enhanced surface-to-volume ratios. Furthermore, heterostructures such as core/shell species[2−5] and mixed metal/semiconductor hybrid systems[6−8] possess additional interfaces with large surface areas.

In all cases, little is known about the nature of associated defects since limited means exist for probing them. However, defects and charges which reside within them strongly influence nanostructure optical properties. As an illustration, both colloidal quantum dot (QD) films and individual nanowires (NWs) exhibit apparent photobrightening effects due to the passivation of surface states through externally introduced charges.[9−12] In particular, occupied traps are prevented from participating in nonradiative relaxation processes experienced by subsequently generated electron−hole pairs. This effectively increases QD film/NW emission quantum yields (QYs). Alternatively, the electric fields of localized charges alter nearby defect state energies, making them less accessible to photogenerated carriers.[13,14] The overall photobrightening effect therefore bears striking resemblance to the emission intensity jumps observed in single QD/NW intermittency studies[15,16] and suggests a connection between the two. Corroborating this, virtually all physical models for nanostructure blinking invoke charging and/or defects.[17] As an added effect, the random motion of long-lived charges on nanostructure surfaces[18] induces a time-dependent Stark effect, which simultaneously rationalizes observed

* Address correspondence to mkuno@nd.edu.

Received for review July 28, 2012 and accepted September 16, 2012.

Published online September 17, 2012
10.1021/nn3033997

single-particle spectral diffusion.[19] This is also the case with nanorods (NRs) where additional biexcitonic shifts are seen.[20,21]

External electric fields likewise alter individual QD,[14] NR,[22] and NW[23] emission intensities. They do so by perturbing defect state energies and/or their occupancy. In QDs, Park *et al.* argue that charge transfer states, which result from trapping processes, possess field-dependent energies. The relative population of exciton *versus* charge transfer states at a given bias then explains observed QY differences.[14] In NRs, external fields interact constructively and destructively with local fields from surface localized carriers, causing reversible emission sensitivities. They also induce carrier detrapping events that result in the appearance of charged exciton emission.[22] Finally, in NWs, Protasenko *et al.* propose that an observed (spatially selective) emission intensity modulation arises from mobile charges that respond to externally applied, in-plane, electric fields.[23] Long-lived charges accumulate and passivate NW trap sites at a given end, causing QYs to increase. In all cases, a point of commonality is the involvement of surface-related traps whose field-influenced occupancy (or vacancy) results in variable nanostructure emission intensities/energies. This highlights the fact that understanding and manipulating charge/defect interactions opens the door to controllably influencing nanostructure optical/electrical properties, which can ultimately lead to applications such as electrochromics, optical modulators, or entirely new classes of devices.

In this article, we study a phenomenon where the emission intensity of individual CdSe NWs is enhanced and modulated by external electric fields applied *perpendicular* to the wire's growth axis. Tangible and reversible QY enhancements of 14 ± 7% are observed in NW emission intensities with applied electric fields ranging from 5 to 22 MV/m. Through a series of ~200 experiments on more than 100 individual NWs, we directly link the effect to field-induced changes of carrier detrapping rates from defect states responsible for nonradiative relaxation processes, namely, a nanoscale Poole–Frenkel effect.[24] To more quantitatively rationalize the phenomenon, we apply a recent model we have developed that describes photogenerated carrier recombination dynamics in CdSe NWs and extend it to account for field-enhanced carrier detrapping rates. What results is a self-consistent explanation for observed quantum yield differences along with asymmetries in the response.

CdSe NWs are embedded in a device that allows them to be subjected to electric fields polarized perpendicular to their growth axis. External fields are generated by applying a potential (V_a) between a transparent indium–tin oxide (ITO) electrode, on which the wires sit, and a grounded gold counter electrode. NWs are separated from the counter electrode by a thin

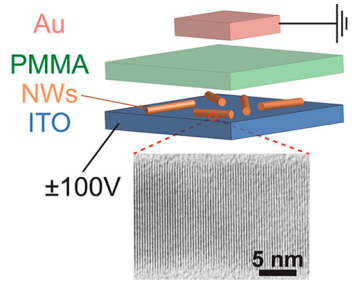

Figure 1. Schematic of the employed device structure. Electric fields are generated by applying a bias between the ITO and a grounded gold counter electrode. The ITO's optical transparency allows for concurrent single NW emission measurements. The image below shows a typical lattice-resolved TEM image of a CdSe NW used in the study.

polymethylmethacrylate (PMMA) layer, 5 ± 0.5 μm thick, as determined from cross-sectional scanning electron microscopy (SEM) (Supporting Information, Figure S1). This geometry has been chosen to minimize potential complications from the field-induced motion of mobile charges along the NW growth axis, previously involved in the spatial and intensity modulation of emission intensities in wires subjected to *in-plane* electric fields.[23] Single NW emission microscopy is simultaneously conducted to investigate variations of the NW photoluminescence intensity.

Figure 1 illustrates both the device structure and the biasing scheme. Contacts to electrodes are made through a home-built probe station, facilitated by drops of eutectic gallium–indium (EGaIn). Under an applied bias of V_a = +100 V (−100 V), field strengths of ~22 MV/m (~5 MV/m) are expected within the NW. Given that built-in fields exist within the device, both external and internal fields are considered in tandem to explain our observations.

We first demonstrate the observed NW emission enhancement/modulation by acquiring emission intensity (I_{em}) time trajectories under an applied bias (V_a) cycled periodically between −100 and +100 V [200 V peak-to-peak (V_{pp})]. A triangle waveform with a frequency of f = 1 Hz is used, with f limited by the CCD framerate (~20 frames per second). Figure 2a shows typical results from these measurements with movies illustrating the effect provided in the Supporting Information. The integrated emission intensity of a single NW (open red circles) follows the applied bias (dashed blue line). Specifically, as V_a increases so too does the NW emission intensity. When V_a decreases, I_{em} drops.

The periodicity of the applied bias is therefore reproduced by the NW emission intensity. This is further corroborated by Figure 2b, which shows the I_{em} trajectory's corresponding Fourier transform. A peak is apparent at the applied modulation frequency, confirming that observed I_{em} changes indeed arise from the applied potential. Interestingly, the NW emission intensity reaches a maximum (minimum) for a positive (negative) bias on the ITO relative to the

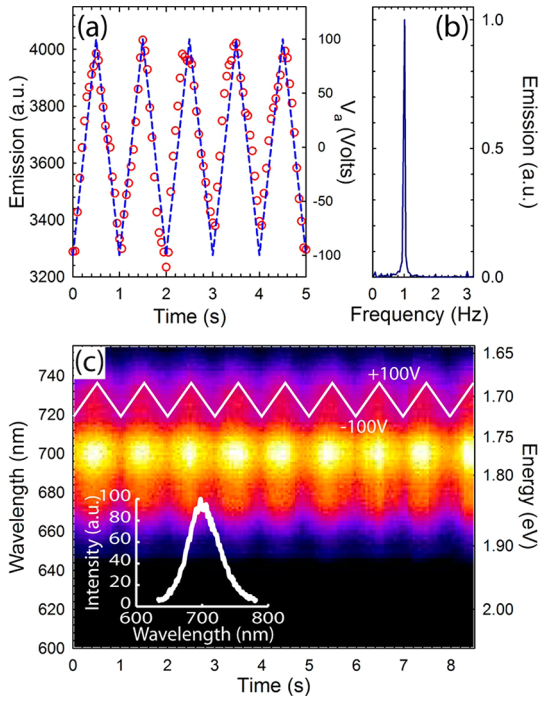

Figure 2. (a) Representative NW emission intensity modulation trajectory (open red circles) acquired using a 200 V_{pp} triangle wave with a 1 Hz frequency (dashed blue line). (b) Corresponding Fourier transform. No modulation is observed at 2f. (c) Complementary NW photoluminescence spectrum trajectory taken under the same applied bias as in (a). The inset shows a representative emission spectrum with an intensity maximum at 700 nm.

grounded gold counter electrode. This asymmetric response can be seen by the absence of any 2*f* contribution to the Fourier transform in Figure 2b, which would arise if maxima (or minima) were observed at *both* positive and negative ITO potentials.

To understand the behavior shown in Figure 2, we must first determine whether charge injection or conversely electric fields are responsible for the I_{em} enhancement/modulation. This is important since the literature suggests that both can dramatically alter colloidal nanostructure optical properties. To discern charging from an electric field effect, we conduct control experiments using an inverted biasing scheme. Instead of applying a positive or negative bias to the ITO (relative to a grounded Au counter electrode), we reverse the scheme. In all cases, NWs remain in direct contact with the ITO. We expect that if charging is responsible for the I_{em} enhancement/modulation it will only occur when the ITO is biased positive or negative. Biasing the gold electrode should yield a negligible response since any injected charges must traverse a ~5 μm insulating dielectric to reach the wires. By contrast, the I_{em} enhancement/modulation effect should remain relatively unaffected in the latter electric field scenario since an E-field will be present in all cases.

In the experiment, we observe that the NW emission is modulated irrespective of whether the ITO or the Au is biased. Furthermore, the NWs exhibit a polarity-dependent reversal of their response along with an I_{em} modulation depth of similar magnitude. Representative data illustrating this can be found in the Supporting Information (Figure S2). These results are nominally expected from the second E-field scenario and are further corroborated by an additional control experiment where introducing an insulating (~20−25 nm) Al_2O_3 buffer layer between the wires and the ITO still results in a response. We conclude that an electric field effect is responsible for the observed I_{em} behavior.

To investigate the possible role of a Stark effect, Figure 2c shows an emission spectrum of a single CdSe NW, monitored in the same fashion as associated I_{em} values in Figure 2a. While the trace shows an apparent NW band edge emission intensity enhancement/modulation, no field-dependent changes to the transition energy are seen. However, since measurements are performed at room temperature, emission peak widths are broad. Given this, we tentatively exclude possible Stark perturbations of emitting states as the origin of the V_a-dependent I_{em} enhancement/modulation.

Next, what's puzzling in Figure 2a is the asymmetric I_{em} response that consists of a clear I_{em} *maximum* at positive V_a and a *minimum* at negative V_a (normal biasing scheme with biases applied to the ITO). This connection between an I_{em} maximum (minimum) and positive (negative) V_a values is robust and holds true for all wires studied. Furthermore, what results from the I_{em} polarity dependence is a 1*f* response, which contrasts to the zeroth order (symmetric) 2*f* response expected for NWs in a capacitor-like structure. Finally, when NW emission intensities on a glass coverslip are compared to estimated QYs within the device at $V_a = 0$ and 100 V, we find that the I_{em} maximum represents a 14 ± 7% QY enhancement relative to the $V_a = -100$ V case.

To rationalize these results and, in particular, the observed asymmetry, we first conduct a detailed analysis of the electric fields experienced by NWs in the device. This involves estimating their one-dimensional potential profile [$\varphi(x)$] by solving Poisson's equation for positive and negative V_a applied to the ITO. The Poisson model provides a limiting approximation to the actual fields experienced by the NWs at the NW/ITO and NW/PMMA interfaces.

For modeling purposes, we consider CdSe NWs to be n-type[25,26] with donor densities ranging from $N_D = 10^{21}$ to 10^{23} m^{-3}.[27,28] In practice, we assume $N_D = 5 \times 10^{23}/m^3$, consistent with defect densities previously invoked to explain the emission intermittency of CdSe NWs.[12] The wires are also assumed to undergo complete Fermi level equilibration with the ITO. Potential confinement-induced conduction and valence band shifts are ignored because mean NW diameters ($d \sim 25$ nm) are large compared to CdSe's bulk exciton Bohr radius ($a_B \sim 5.6$ nm). The Supporting Information

provides an illustration of the assumed electron affinities, ionization potentials, and Fermi levels for each layer in the device (Figure S3). Associated Poisson equations, boundary conditions, and solutions within the depletion approximation are also provided.

From this analysis, we find that E-field strengths at the NW center range from ~5 to ~22 MV/m. Even under zero external bias, an electric field exists within the NW due to the built-in field at the NW/ITO interface. Its magnitude is 1.37×10^7 V/m (*i.e.*, 1.37×10^5 V/cm), and only with large negative V_a values (*i.e.*, $V_a < -100$ V) is the field completely zero inside the wire.

The most important outcome of the model is its prediction of an asymmetric E-field response. Specifically, the largest field experienced by the NW occurs when V_a is positive (*i.e.*, $V_a = +100$ V, $|E_{field}| \sim 22$ MV/m). Conversely, the smallest E-field magnitude occurs when the applied bias is negative (*i.e.*, $V_a = -100$ V, $|E_{field}| \sim 5$ MV/m). A plot illustrating this can be found in the Supporting Information, Figures S4 and S5. As a consequence, this asymmetric response explains the 1*f* enhancement/modulation effect seen earlier in Figure 2.

Given an origin for the V_a-dependent asymmetry as well as associated electric field strengths, we now focus on the physical mechanism behind the I_{em} enhancement/modulation in order to explain the I_{em} V_a polarity dependence as well as the QY enhancement on applying a positive potential to the ITO. We posit that applying an external field causes reversible variations of carrier detrapping rates from NW defect states responsible for nonradiative relaxation processes. In bulk materials, this is known as the Poole–Frenkel effect.[29,30] Its underlying physical basis is the field-induced lowering of barrier heights for trapped charges. This increases detrapping rates and enables carriers to return to their associated conduction/valence bands whereupon they can recombine radiatively with counterpart charges. The Poole–Frenkel effect is illustrated schematically in Figure 3a. In the case of transport measurements, this barrier height lowering leads to a corresponding field-dependent carrier mobility, which accounts for exponential increases in conductivity with applied field strength.[31]

Note that the Poole–Frenkel effect invokes charged defect states because this is the origin of a Coulomb barrier, which prevents carrier detrapping. For electrons, a positively charged trap is needed; for holes, traps must be negatively charged. In CdSe, previous bulk studies have identified single or double negatively charged defects as dominant sensitization centers. These acceptor sites occur with a range of energies 0.10–0.75 eV above the valence band.[32–36] They are thought to be native defects of the material related to Cd vacancies that leave exposed Se ions to act as hole traps.[33] Associated hole capture cross sections are large, $\sim 10^{-14}$ cm^2, with accompanying electron

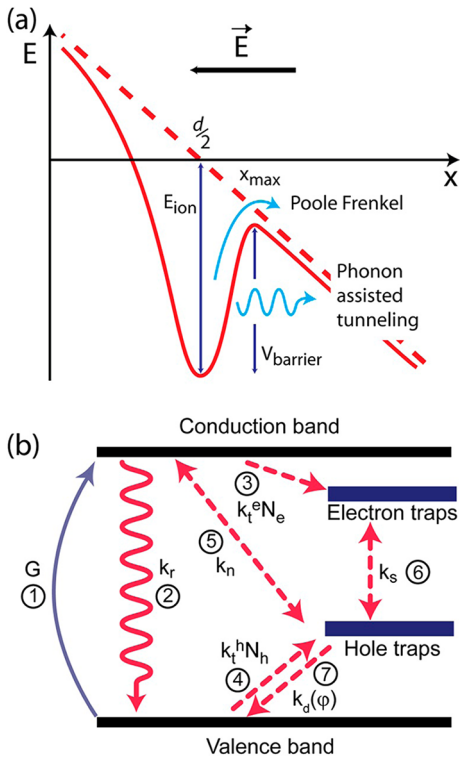

Figure 3. (a) Electric field-enhanced carrier detrapping mechanisms. They include the Poole–Frenkel effect, which involves a field-induced barrier height lowering followed by subsequent thermionic emission, and phonon assisted tunneling, aided by the corresponding field-induced barrier width reduction. (b) Schematic of a kinetic model used to rationalize electric field-enhanced carrier detrapping rates, leading to NW QY variations.

capture cross sections between 10^{-18} and 10^{-21} cm^2.[37] In what follows, we consider a nominal hole trap depth of 0.35 eV to model relatively shallow traps responsive to the modest E-fields in the experiment.

The importance of acceptor states in CdSe nanostructure photophysics is supported by theoretical tight-binding studies of ligand-passivated CdSe QDs, which show deep Se dangling bond hole traps in nanocrystals with reconstructed surfaces.[38] Optically detected magnetic resonance (ODMR) experiments on CdSe nanocrystals, using emission red-shifted from the band edge, support this and reveal line shapes best reproduced by carriers residing in both shallow donor and deep acceptor sites.[39] This is further corroborated by ensemble fluorescence upconversion[40] as well as photobrightening studies,[41] which highlight the importance of hole traps in determining nanocrystal quantum yields.

Invoking a nanoscale Poole–Frenkel effect as the root cause of the observed phenomenon, we estimate its effect on CdSe NW QYs. This is done by modifying a previously developed kinetic model for NWs[42] that takes into account the key role played by hole trapping in determining NW[42] and QD[43] QYs. The model also successfully accounts for the superlinear growth of the

NW emission intensity with excitation intensity, the observation of variable emission quantum yields (values ranging from 0.1 to 20%), excited state lifetimes on the order of 100−500 ps, and ensemble transient differential absorption kinetics showing nanosecond time scales.[42]

Figure 3b summarizes the model's level scheme along with its associated rate processes and time constants. NW excitation is shown as process 1. Subsequent bimolecular electron−hole radiative relaxation (process 2) competes with slow electron trapping into donor states (process 3), fast hole trapping into acceptor states (process 4), free electron recombination with trapped holes (process 5), and trapped electron-trapped hole recombination (process 6), all nonradiative processes. To account for Poole−Frenkel enhanced hole detrapping, we include process 7.

The following rate equations summarize the model

$$\frac{dn}{dt} = G - k_r np - k_n np_t - k_t^e N_e n \quad (1)$$

$$\frac{dp}{dt} = G - k_r np - k_t^h N_h p + k_d(\varphi) p_t \quad (2)$$

$$\frac{dn_t}{dt} = k_t^e N_e n - k_s n_t p_t \quad (3)$$

$$\frac{dp_t}{dt} = k_t^h N_h p - k_n np_t - k_s n_t p_t - k_d(\varphi) p_t \quad (4)$$

where n (p) is the electron (hole) linear concentration (number/unit length), n_t (p_t) are their trapped concentrations (number/unit length), G is the generation rate ($G = (I_{exc}\sigma_{abs})/(h\nu)$, 1/s·unit length), σ_{abs} is the NW absorption cross section,[44] k_r (k_n) is the second-order radiative recombination rate constant (second-order rate constant describing the recombination of free electrons and trapped holes), k_t^e (k_t^h) is the second-order rate constant for electron (hole) trapping, and k_s is the rate constant describing the nonradiative recombination of trapped electrons and holes. N_e (N_h) is the electron (hole) trap density (number per unit length), assuming that the majority of traps are not filled (*i.e.*, $N_h \gg p_t$ and $N_e \gg n_t$). For quantitative estimates, the following rate constants are assumed based on experimental time-correlated single-photon counting and transient differential absorption measurements on CdSe NWs as well as literature values: $k_t^h N_h \sim 100$ ns^{-1} (1×10^{11} s^{-1}), $k_t^e N_e \sim 0.01$ ns^{-1} (1×10^7 s^{-1}), $k_n \sim 0.0032$ μm ns^{-1} (3.2×10^2 cm s^{-1}), $k_r \sim 0.01$ μm ns^{-1} (1×10^3 cm s^{-1}), and $k_s \sim 0.0001$ μm ns^{-1} (10 cm s^{-1}).[42]

In the absence of known hole detrapping rates in CdSe, we approximate the zero field rate using $k_d^0 = \sigma_t(g_0/g_1)\langle v_{th}\rangle N_v \exp(-qE_{ion}/kT)$,[45] where $\sigma_t = 10^{-14}$ cm^2 is the hole capture cross section,[32] $g_0 = 1$ and $g_1 = 2$ are trap state degeneracies before and after detrapping,[46] $v_{th} = (3kT/m^*)^{1/2} = 1.7 \times 10^5$ m/s is the hole thermal velocity assuming $m^* = 0.45\ m_o$, $N_v = 2(2\pi m^* kT/h^2)^{3/2} = 7.45 \times 10^{24}$ m^{-3} is the effective bulk valence band density of states, and $E_{ion} = 0.35$ eV is the trap state ionization energy in eV.[32] The expression originates in deep level transient spectroscopy[45,47] and provides good estimates of carrier emission rates. An explicit zero field detrapping rate is $k_d^0 = 7.74 \times 10^5$ s^{-1}.

In the presence of an external field, the Poole−Frenkel effect alters k_d^0 by reducing trap barrier heights. The magnitude of this barrier height lowering can be estimated using a 1D Poole−Frenkel model. Specifically, in a homogeneous electric field, the trapped charge's potential energy is $V(x) = -q^2/(4\pi\varepsilon\varepsilon_0 x) - q|E_{field}|x$, where q is the elementary charge, ε is the NW's relative permittivity ($\varepsilon = 8.2$),[48] ε_0 is the vacuum permittivity, and $|E_{field}|$ is the applied field strength. The barrier maximum therefore occurs at $x_{max} = (q/4\pi\varepsilon\varepsilon_0|E_{field}|)^{1/2}$ and yields a potential barrier maximum of $V(x_{max}) = -q(q|E_{field}|/\pi\varepsilon\varepsilon_0)^{1/2}$ that is sensitive to the square root of the electric field. In practice, since the electric field within the NW is not homogeneous, we use $V(x) = -q^2/(4\pi\varepsilon\varepsilon_0 x) + q\varphi(x)$, where $\varphi(x)$ is the potential obtained from our earlier Poisson analysis of the NW device (Supporting Information). Solving for $V'(x)$=0 gives x_{max} and $V(x_{max})$ from where the corresponding barrier height in Joules is $V_{barrier} = V(x_{max}) - [q\varphi(d/2) - qE_{ion}]$. For simplicity, the trap is assumed to be halfway between the NW/ITO and NW/PMMA interfaces.

Detrapping rate variations can subsequently be estimated using an enhancement factor, $\eta = \exp((qE_{ion} - V_{barrier})/kT)$, which represents the ratio of Boltzmann factors with and without the external field. This leads to a field-dependent detrapping rate of $k_d(\varphi) = k_d^0\eta$. Applying an electric field of $|E_{field}| \sim 22$ MV/m therefore results in an effective barrier height lowering of ~128 meV (relative to the zero field case), an enhancement factor of $\eta \sim 146$, and an effective hole detrapping rate of $k_d = 1.13 \times 10^8$ s^{-1}. Details of these estimates as well as a plot of k_d *versus* φ can be found in the Supporting Information (Figures S6−S9).

We now use $k_d(\varphi)$ in our kinetic model to obtain predicted emission intensities and QYs at modest excitation intensities, I_{exc}. We assume $I_{exc} \sim 10^3$ W/cm^2 as well as a nominal absorption cross section of $\sigma_{abs} = 10^{-10}$ cm^2 μm^{-1}.[44] Equations 1−4 are then solved numerically to yield a steady-state emission intensity, $I_{em} = k_r np$, where I_{em} implicitly assumes free carrier rather than excitonic emission in the large-diameter NWs used here.[42] The model predicts nominal zero external field QYs on the order of 2%, in line with previous observations.[42]

For completeness, we simultaneously investigate whether phonon-assisted tunneling (PAT) contributes to k_d when $|E_{field}|$ is sufficiently large. This is because both the barrier height and width are reduced on applying an external field (Figure 3a). Details about the calculation of phonon-assisted tunneling rates can

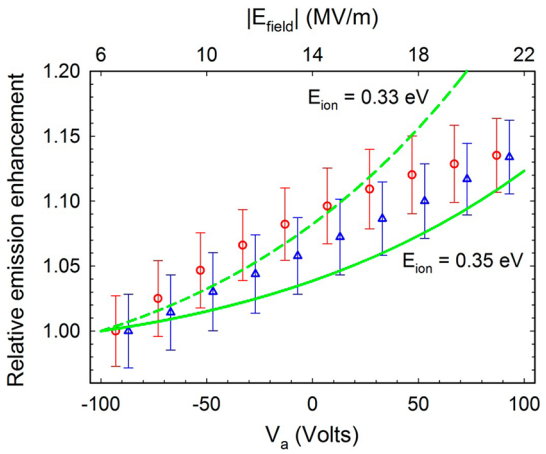

Figure 4. Experimental single NW emission intensities scaled to the −100 V I_{em} value under increasing [decreasing] bias (open red circles) [open blue triangles]. Also plotted are similarly scaled model I_{em} values for nominal trap depths of E_{ion} = 0.35 and 0.33 eV (solid green line and dashed green line, respectively). Error bars represent the standard deviation in multiple voltage sweeps of a single NW.

be found in the Supporting Information. We find that the total detrapping enhancement factor (*i.e.*, the sum of Poole−Frenkel and PAT contributions) remains effectively unchanged. This allows us to conclude that phonon-assisted tunneling does not play a significant role in the observed phenomenon. Pure tunneling is not considered since it is only important at low temperatures or with fields in excess of 1 GV/m.[29]

At this point, Figure 4 shows the qualitative agreement that results between experiment and theory. When $V_a = -100$ V, the predicted QY is 2.33%. As the external bias increases toward $V_a = +100$ V, the predicted QY rises to QY = 2.62%. The resulting quantum yield enhancement relative to the $V_a = -100$ V value is therefore ∼12%. This agrees with the experimental results shown in Figure 4 and with data taken over 100 NWs (*i.e.*, a 14 ± 7% modulation of the QY between $V_a = -100$ and +100 V). The model therefore reproduces both the I_{em} polarity dependence as well as the observed 1*f* response of the wires. Note that in the comparison all experimental and theoretical results have been scaled by their respective $V_a = -100$ V I_{em} values. This is because the Poisson analysis shows that an electric field exists within a NW at all times even when $V_a = 0$. Only when V_a is sufficiently negative does the field magnitude inside the wire equal zero.

Unfortunately, a true quantitative comparison between experiment and theory is not possible because the magnitudes of actual hole trap depths within CdSe NWs are not known. While we have assumed E_{ion} = 0.35 eV to represent states readily influenced by E-fields in the experiment, we also illustrate the model's sensitivity to trap depths by plotting the predicted response for E_{ion} = 0.33 eV. Independent information about NW hole trap depths and their distributions within the gap is therefore needed.

Figure 4 also reveals another difference between experiment and theory. Namely, the field-dependent detrapping enhancement possesses a convex appearance (*i.e.*, it grows rapidly as V_a approaches +100 V). By contrast, the experiment tends toward a concave trend. This is most apparent in forward bias sweeps where V_a increases from −100 to +100 V (open red circles). It is less evident in reverse sweeps where V_a decreases from +100 to −100 V (open blue triangles).

There are several possible origins for this (concave) curvature. One is the field-induced spatial separation of electron and hole wave functions which decreases their overlap at large field strengths and leads to a corresponding quenching of the emission. A rolloff of the Poole−Frenkel response at high fields can therefore occur. Alternatively, mobile charges in the system, stemming from what are likely surface-localized charges, can redistribute themselves at large field strengths to screen the wires. Such charges have previously been observed to influence the emission intensities of NWs subjected to in-plane electric fields.[23] There is some evidence for this possibility here since holding the potential constant at $V_a = +100$ V (or $V_a = -100$ V) should lead to a continuously enhanced (suppressed) emission QY. In practice, though, we find that the experimental I_{em} enhancement/suppression is metasable and slowly decays over the course of seconds. This is illustrated in Figure S10 of the Supporting Information. Additional studies about this relaxation mechanism are therefore needed to fully explain the NW response. Despite this, the observation of a Poole−Frenkel effect in the emission from single NWs represents a first step toward developing optical assays to probe defects in low-dimensional materials.

CONCLUSION

We have observed a reversible emission enhancement/modulation phenomenon in single CdSe NWs upon applying an external bias. The emission sensitivity is rationalized by the field-induced modulation of carrier detrapping rates from defect sites responsible for nonradiative relaxation processes in the wires. The underlying physical mechanism is a nanoscale Poole−Frenkel effect which lowers trap state barriers and enhances carrier detrapping events. Subsequent modeling of the electric fields and potentials experienced by the NW explains the origin of an asymmetric V_a response where an emission maximum (minimum) is observed under positive (negative) bias applied to the ITO substrate on which the wires sit. The observation is further rationalized by invoking a kinetic model previously developed to understand CdSe NW carrier dynamics and by accounting for field-dependent detrapping rates. The good qualitative agreement between experiment and theory suggests that the

observed NW I_{em} enhancement/modulation phenomenon offers insight into hole trapping dynamics in CdSe nanowires and potentially opens the door to new single-particle trap state spectroscopies that can help clarify, mitigate, and possibly exploit the impact of defects in low-dimensional materials.

MATERIALS AND METHODS

Materials. CdSe NWs were prepared using solution−liquid−solid growth.[49,50] Briefly, this entails mixing cadmium oxide (CdO, 25 mg, Sigma Aldrich, 99.99%) and myristic acid (0.662 g, Sigma Aldrich, 99%) in trioctylphosphine oxide (TOPO, 2 g, Strem, 99%). The mixture is then heated and degassed at ∼100 °C for 50 min. Once complete, the temperature is raised to 260 °C whereupon the solution turns clear. An injection solution consisting of 1 M trioctylphosphine selenide [TOPSe, 25 μL, 25 μmol, made by mixing TOP (Sigma Aldrich, 90%) and Se powder (Sigma Aldrich, 99.5%)], 0.2 mL trioctylphosphine (TOP), and 40 mM $BiCl_3$ (25 μL, 1 μmol, Acros Organics, 98% anh., in acetone) is introduced to initiate the reaction. Wires are grown at temperatures between T = 250 and 300 °C for approximately 2 min before the reaction is quenched. Toluene is added to prevent TOPO from solidifying. NWs are precipitated from solution by adding methanol and are recovered by centrifuging the resulting suspension. Subsequent washing steps expose the recovered precipitate to a mixture of toluene and methanol to remove any excess TOPO. Recovered NWs are stored in toluene. Representative NW TEM images can be found in the Supporting Information (Figure S11). More details about these synthesis/purification protocols can be found in ref 51. Additional details about the crystal structure and morphology of resulting wires can be found in refs 49, 50, and 52.

Device Preparation. A dilute solution of NWs is drop-cast onto ITO (SPI, 8−12 Ω or Delta Technologies, 15−25 Ω) coverslips. A thin layer (5 ± 0.5 μm) of PMMA (75 000 MW, Polysciences) is then deposited over the wires through spin-coating (2000 rpm) from a 25 wt % solution of PMMA in anisole. Small (∼0.1 in. diameter) gold pads (∼200 nm thickness) are sputtered (Emitech) on top of the PMMA using home-built masks, made of sheet metal. Masks consist of 3 × 3 arrays of holes (∼0.09 in. diameter) that enable us to prepare nine devices for each ITO substrate used.

Optical Measurements and Electrical Biasing. Single-wire emission measurements are conducted using a home-built single-molecule imaging system, based on an inverted optical microscope (Nikon). NWs are excited at one of three frequencies, 405 nm (Coherent), 473 nm (Oxxius), or 532 nm (Power Technology). The excitation is focused with a high numerical aperture objective (Zeiss, 63×, 0.65 NA). For wide-field measurements, a 40 cm focal length lens is placed prior to the objective's back aperture. This yields a ∼35 μm diameter excitation spot on the substrate. Excitation intensities are adjusted using two crossed polarizers to yield levels of ∼1000 W/cm^2. Emitted light from a given NW is then collected with the same objective and is passed through a 570 nm long-pass filter (Chroma). This light is subsequently imaged using an EMCCD camera (Andor) to record intensity trajectories. To measure emission spectra, an imaging spectrometer (Acton) is added prior to the CCD camera. This also allows emission spectra trajectories to be acquired.

Biases are applied using a home-built probe station placed atop the microscope. Drops of EGaIn ensure ohmic contacts. In the default biasing scheme, a 1 Hz triangle wave from a function generator (Tektronics) is amplified to 200 V_{pp} using a home-built 20× voltage amplifier. It is then applied to the ITO with the Au counter electrode grounded. For control measurements, the biasing scheme is reversed.

During modulation experiments, the NW emission intensity is monitored as a function of applied bias. Twenty points are recorded for every period of the applied waveform. While the function generator's first channel generates the triangle wave, its second channel externally triggers the CCD at a 20 fps frame rate; 512 points are collected in every trace with two traces taken for each wire. The first trace represents the I_{em} trajectory, obtained using our default biasing scheme. The second trace is taken with the biasing reversed. Control measurements are recorded to verify constant laser intensities during these trajectories. This entails removing the 570 nm long-pass filter and monitoring the attenuated laser output directly with the EMCCD.

Conflict of Interest: The authors declare no competing financial interest.

Acknowledgment. T.T. thanks the Fulbright Foundation for a visiting scholar grant. M.K. acknowledges financial support from the NSF CAREER program (CHE-0547784). M.K. and B.J. also thank the NSF for partial funding of this study through the NIRT program (ECS-0609249). Additional support from the Notre Dame Radiation Laboratory and the DOE Office of Basic Energy Sciences is acknowledged. We thank Rick Morasse for assistance with the sample preparation, Jixin Si for useful discussions, and Matthew P. McDonald for critically reviewing the manuscript.

Supporting Information Available: Cross-sectional SEM images of the device, movies illustrating the I_{em} enhancement/modulation phenomenon, I_{em} modulation traces acquired using an inverted biasing scheme, device level scheme as well as results of a 1D Poisson model, table of assumed model parameters, plot of the resulting bias-dependent E-field asymmetry, Poole−Frenkel enhancement factor estimate and plot of k_d *versus* V_a, metastable I_{em} enhancement/modulation plot, and representative high-resolution TEM images of CdSe NWs. This material is available free of charge *via* the Internet at http://pubs.acs.org.

REFERENCES AND NOTES

1. Shockley, W.; Read, W. T. Statistics of the Recombinations of Holes and Electrons. *Phys. Rev.* **1952**, *87*, 835–842.
2. Hines, M. A.; Guyot-Sionnest, P. Synthesis and Characterization of Strongly Luminescing ZnS-Capped CdSe Nanocrystals. *J. Phys. Chem.* **1996**, *100*, 468–471.
3. Dabbousi, B. O.; Rodriguez-Viejo, J.; Mikulec, F. V.; Heine, J. R.; Mattoussi, H.; Ober, R.; Jensen, K. F.; Bawendi, M. G. (CdSe)ZnS Core−Shell Quantum Dots: Synthesis and Characterization of a Size Series of Highly Luminescent Nanocrystallites. *J. Phys. Chem. B* **1997**, *101*, 9463–9475.
4. Goebl, J. A.; Black, R. W.; Puthussery, J.; Giblin, J.; Kosel, T. H.; Kuno, M. Solution-Based II−VI Core/Shell Nanowire Heterostructures. *J. Am. Chem. Soc.* **2008**, *130*, 14822–14833.
5. Li, Z.; Ma, X.; Sun, Q.; Wang, Z.; Liu, J.; Zhu, Z.; Qiao, S. Z.; Smith, S. C.; Lu, G.; Mews, A. Synthesis and Characterization of Colloidal Core−Shell Semiconductor Nanowires. *Eur. J. Inorg. Chem.* **2010**, *27*, 4325–4331.
6. Mokari, T.; Rothenberg, E.; Popov, I.; Costi, R.; Banin, U. Selective Growth of Metal Tips onto Semiconductor Quantum Rods and Tetrapods. *Science* **2004**, *304*, 1787–1790.
7. Amirav, L.; Alivisatos, A. P. Photocatalytic Hydrogen Production with Tunable Nanorod Heterostructures. *J. Phys. Chem. Lett.* **2010**, *1*, 1051–1054.
8. Talapin, D. V.; Yu, H.; Shevchenko, E. V.; Lobo, A.; Murray, C. B. Synthesis of Colloidal PbSe/PbS Core−Shell Nanowires and PbS/Au Nanowire−Nanocrystal Heterostructures. *J. Phys. Chem. C* **2007**, *111*, 14049–14054.
9. Tice, D. B.; Frederick, M. T.; Chang, R. P. H.; Weiss, E. A. Electron Migration Limits the Rate of Photobrightening in Thin Films of CdSe Quantum Dots in a Dry N-2 (g) Atmosphere. *J. Phys. Chem. C* **2011**, *115*, 3654–3662.
10. Schafer, S.; Wang, Z.; Kipp, T.; Mews, A. Fluorescence Modulation of Single CdSe Nanowires by Charge Injection through the Tip of an Atomic-Force Microscope. *Phys. Rev. Lett.* **2011**, *107*, 137403-1–137403-5.

11. Yu, M.; Van Orden, A. Enhanced Fluorescence Intermittency of CdSe−ZnS Quantum-Dot Clusters. *Phys. Rev. Lett.* **2006**, *97*, 237402-1–237402-4.
12. Glennon, J. J.; Buhro, W. E.; Loomis, R. A. Simple Surface-Trap-Filling Model for Photoluminescence Blinking Spanning Entire CdSe Quantum Wires. *J. Phys. Chem. C* **2008**, *112*, 4813–4817.
13. Maenosono, S. Modeling Photoinduced Fluorescence Enhancement in Semiconductor Nanocrystal Arrays. *Chem. Phys. Lett.* **2003**, *376*, 666–670.
14. Park, S.-J.; Link, S.; Miller, W. L.; Gesquiere, A.; Barbara, P. F. Effect of Electric Field on the Photoluminescence Intensity of Single CdSe Nanocrystals. *Chem. Phys.* **2007**, *341*, 169–174.
15. Nirmal, M.; Dabbousi, B. O.; Bawendi, M. G.; Macklin, J. J.; Trautman, J. K.; Harris, T. D.; Brus, L. E. Fluorescence Intermittency in Single Cadmium Selenide Nanocrystals. *Nature* **1996**, *383*, 802–804.
16. Protasenko, V. V.; Hull, K. L.; Kuno, M. Disorder-Induced Optical Heterogeneity in Single CdSe Nanowires. *Adv. Mater.* **2005**, *17*, 2942–2949.
17. Frantsuzov, P.; Kuno, M.; Janko, B.; Marcus, R. A. Universal Emission Intermittency in Quantum Dots, Nanorods and Nanowires. *Nat. Phys.* **2008**, *4*, 519–522.
18. Empedocles, S. A.; Bawendi, M. G. Influence of Spectral Diffusion on the Line Shapes of Single CdSe Nanocrystallite Quantum Dots. *J. Phys. Chem. B* **1999**, *103*, 1826–1830.
19. Empedocles, S. A.; Bawendi, M. G. Quantum-Confined Stark Effect in Single CdSe Nanocrystallite Quantum Dots. *Science* **1997**, *278*, 2114–2117.
20. Muller, J.; Lupton, J. M.; Rogach, A. L.; Feldmann, J.; Talapin, D. V.; Weller, H. Monitoring Surface Charge Migration in the Spectral Dynamics of Single CdSe/CdS Nanodot/Nanorod Heterostructures. *Phys. Rev. B* **2005**, *72*, 205339-1–205339-12.
21. Muller, J.; Lupton, J. M.; Rogach, A. L.; Feldmann, J.; Talapin, D. V.; Weller, H. Monitoring Surface Charge Movement in Single Elongated Semiconductor Nanocrystals. *Phys. Rev. Lett.* **2004**, *93*, 167402-4.
22. Rothenberg, E.; Kazes, M.; Shaviv, E.; Banin, U. Electric Field Induced Switching of the Fluorescence of Single Semiconductor Quantum Rods. *Nano Lett.* **2005**, *5*, 1581–1586.
23. Protasenko, V.; Gordeyev, S.; Kuno, M. Spatial and Intensity Modulation of Nanowire Emission Induced by Mobile Charges. *J. Am. Chem. Soc.* **2007**, *129*, 13160–13171.
24. Frenkel, J. On Pre-breakdown Phenomena in Insulators and Electronic Semi-conductors. *Phys. Rev.* **1938**, *54*, 647–648.
25. Doh, Y.-J.; Maher, K. N.; Ouyang, L.; Yu, C. L.; Park, H.; Park, J. Electrically Driven Light Emission from Individual CdSe Nanowires. *Nano Lett.* **2008**, *8*, 4552–4556.
26. Khandelwal, A.; Jena, D.; Grebinski, J. W.; Hull, K. L.; Kuno, M. Ultrathin CdSe Nanowire Field-Effect Transistors. *J. Electron. Mater.* **2006**, *35*, 170–172.
27. Btirmeister, R. A.; Stevenson, D. A. Electrical Properties of n-Type CdSe. *Phys. Status Solidi B* **1967**, *24*, 683–694.
28. Kindleysides, L.; Woods, J. Electron Traps in Cadmium Selenide. *J. Phys. D: Appl. Phys.* **1970**, *3*, 451–461.
29. Martin, P. A.; Streetman, B. G.; Hess, K. Electric-Field Enhanced Emission from Non-Coulombic Traps in Semiconductors. *J. Appl. Phys.* **1981**, *52*, 7409–7415.
30. Ganichev, S. D.; Ziemann, E.; Prettl, W.; Yassievich, I. N.; Istratov, A. A.; Weber, E. R. Distinction between the Poole−Frenkel and Tunneling Models of Electric-Field-Stimulated Carrier Emission from Deep Levels in Semiconductors. *Phys. Rev. B* **2000**, *61*, 10361–10365.
31. Katzenmeyer, A. M.; Leonard, F.; Talin, A. A.; Wong, P.-S.; Huffaker, D. L. Poole−Frenkel Effect and Phonon-Assisted Tunneling in GaAs Nanowires. *Nano Lett.* **2010**, *10*, 4935–4938.
32. Ture, I. E.; Poulin, F.; Brinkman, A. W.; Woods, J. Electron Traps and Deep Levels in Cadmium Selenide. *Phys. Status Solidi A* **1983**, *77*, 535–544.
33. Ture, I. E.; Claybourn, M.; Brinkman, A. W.; Woods, J. Defects in Cadmium Selenide. *J. Cryst. Growth* **1985**, *72*, 189–193.
34. Robinson, A. L.; Bube, R. H. Photoelectronic Properties of Defects in CdSe Single Crystals. *J. Appl. Phys.* **1971**, *42*, 5280–5295.
35. Manfredotti, C.; Murri, R.; Pepe, E.; Semisa, D. Photoelectronic Properties of Photoconducting CdSe. *Phys. Status Solidi A* **1973**, *20*, 477–486.
36. Smyntyna, V. A. Centers of Slow Recombination in Single-Crystal Cadmium Selenide Films. *Sov. Phys. Semicond.* **1983**, *17*, 424–426.
37. Bube, R. H. Cross-Section Ratios of Sensitizing Centers in Photoconductors. *J. Appl. Phys.* **1961**, *32*, 1707–1709.
38. Pokrant, S.; Whaley, K. B. Tight-Binding Studies of Surface Effects on Electronic Structure of CdSe Nanocrystals: The Role of Organic Ligands, Surface Reconstruction, and Inorganic Capping Shells. *Eur. Phys. J. D* **1999**, *6*, 255–267.
39. Lifshitz, E.; Dag, I.; Litvitn, I. D.; Hodes, G. Optically Detected Magnetic Resonance Study of Electron/Hole Traps on CdSe Quantum Dot Surfaces. *J. Phys. Chem. B* **1998**, *102*, 9245–9250.
40. Underwood, D. F.; Kippeny, T.; Rosenthal, S. J. Ultrafast Carrier Dynamics in CdSe Nanocrystals Determined by Femtosecond Fluorescence Upconversion Spectroscopy. *J. Phys. Chem. B* **2001**, *105*, 436–443.
41. Jasieniak, J.; Mulvaney, P. From Cd-Rich to Se-Rich—The Manipulation of CdSe Nanocrystal Surface Stoichiometry. *J. Am. Chem. Soc.* **2007**, *129*, 2841–2848.
42. Vietmeyer, F.; Frantsuzov, P. A.; Janko, B.; Kuno, M. Carrier Recombination Dynamics in Individual CdSe Nanowires. *Phys. Rev. B* **2011**, *83*, 115319-1–115319-10.
43. Knowles, K. E.; McArthur, E. A.; Weiss, E. A. A Multi-Timescale Map of Radiative and Nonradiative Decay Pathways for Excitons in CdSe Quantum Dots. *ACS Nano* **2011**, *5*, 2026–2035.
44. Giblin, J.; Kuno, M. Nanostructure Absorption: A Comparative Study of Nanowire and Colloidal Quantum Dot Absorption Cross Sections. *J. Phys. Chem. Lett.* **2010**, *1*, 3340–3348.
45. Bourgoin, J.; Lannoo, M. *Point Defects in Semiconductors*; Springer: New York, 1983.
46. Manfredotti, C.; Rizzo, A.; Vasanelli, L.; Galassini, S.; Ruggiero, L. Electron Trapping Levels in Cadmium Selenide Single-Crystals. *J. Appl. Phys.* **1973**, *44*, 5463–5469.
47. Dobaczewski, L.; Peaker, A. R.; Bonde Nielsen, K. Laplace-Transform Deep-Level Spectroscopy: The Technique and Its Applications to the Study of Point Defects in Semiconductors. *J. Appl. Phys.* **2004**, *96*, 4689–4728.
48. Krauss, T. D.; Brus, L. E. Charge, Polarizability, and Photoionization of Single Semiconductor Nanocrystals. *Phys. Rev. Lett.* **1999**, *83*, 4840–4843.
49. Wang, F.; Dong, A.; Sun, J.; Tang, R.; Yu, H.; Buhro, W. E. Solution-Liquid-Solid Growth of Semiconductor Nanowires. *Inorg. Chem.* **2006**, *45*, 7511–7521.
50. Kuno, M. An Overview of Solution-Based Semiconductor Nanowires: Synthesis and Optical Studies. *Phys. Chem. Chem. Phys.* **2008**, *10*, 620–639.
51. Puthussery, J.; Kosel, T. H.; Kuno, M. Facile Synthesis and Size Control of II−VI Nanowires Using Bismuth Salts. *Small* **2009**, *5*, 1112–1116.
52. Grebinski, J. W.; Hull, K. L.; Zhang, J.; Kosel, T. H.; Kuno, M. Solution-Based Straight and Branched CdSe Nanowires. *Chem. Mater.* **2004**, *16*, 5260–5272.